

Solving Sub-Wavelength Lattice Reduction in Full-Metal Front-Ends for Dual-Polarized Active Antennas

Lucas Polo-López, Esteban Menargues, Santiago Capdevila, Giovanni Toso, Maria Garcia-Vigueras

▶ **To cite this version:**

Lucas Polo-López, Esteban Menargues, Santiago Capdevila, Giovanni Toso, Maria Garcia-Vigueras. Solving Sub-Wavelength Lattice Reduction in Full-Metal Front-Ends for Dual-Polarized Active Antennas. IEEE Transactions on Antennas and Propagation, 2022, 70 (9), pp.7413-7426. 10.1109/TAP.2022.3198512 . hal-03827268

HAL Id: hal-03827268
https://hal.science/hal-03827268

Submitted on 15 Dec 2022

HAL is a multi-disciplinary open access archive for the deposit and dissemination of scientific research documents, whether they are published or not. The documents may come from teaching and research institutions in France or abroad, or from public or private research centers.

L'archive ouverte pluridisciplinaire **HAL**, est destinée au dépôt et à la diffusion de documents scientifiques de niveau recherche, publiés ou non, émanant des établissements d'enseignement et de recherche français ou étrangers, des laboratoires publics ou privés.

This article has been accepted for publication in IEEE Transactions on Antennas and Propagation. This is the author's version which has not been fully edited and content may change prior to final publication. Citation information: DOI 10.1109/TAP.2022.3198512

Solving Sub-wavelength Lattice Reduction in Full-metal Front-ends for Dual-polarized Active Antennas

Lucas Polo-López, Esteban Menargues, Santiago Capdevila, Giovanni Toso, *Senior Member, IEEE* and María García-Vigueras, *Member, IEEE,*

***Abstract*—This paper proposes an original structure of evanescent quad-ridge antenna to conceive dual-polarized full-metal front-ends that can be used in active antennas with wide field-of-view. An original design methodology is here proposed that allows to induce radiation from sub-wavelength squared apertures based on the use of evanescent and quad-ridge waveguides. The proposal is illustrated by means of a design with 4.5% bandwidth providing dual-circular polarization with good performance up to 50°-scanning even in the diagonal plane. For comparison purposes, a metallic benchmark is also proposed, which is based on the use of classical quad-ridge horns. Such comparative analysis allows to understand the superior performance of the proposed concept and its main advantage: it allows to avoid the excitation of the first high order mode in the squared quad-ridge aperture. The excitation of such spurious mode in the antenna is explained in terms of simple equivalent circuit models characterizing the aperture periodic discontinuity.**

***Index Terms*—Active antennas, phased arrays, sub-wavelength radiating apertures, satellite antennas, periodic discontinuity circuit modelling.**

I. Introduction

FLEXIBILITY enhancement in space-borne payloads is a requirement becoming more and more important recently [1]. In the near future it is expected that new payloads can evolve and re-adapt to new market needs during satellite lifetime. The use of active antennas (AAs) allows to attain such reconfigurability, since they can change the shape, position and power level of their beams [2]. Additionally, when implemented as Direct Radiating Arrays (DRA), AAs have the potential for avoiding cumbersome mechanical and/or deploying mechanisms [3].

One of the most demanded reconfiguration capabilities is the possibility of steering the radiation pattern. Low Earth Orbit (LEO) satellite applications typically require a $\pm 50^{\circ}$ field of view (FoV) [4]. The steering requirements for ground terminals are also similar. The maximum scanning angle that can be achieved by any antenna array is limited by the well-known theoretical limit associated to the appearance of grating lobes (GL) [5]. Among other disadvantages, such undesired radiated lobes may reduce the antenna efficiency, create interference and violate ITU (International Telecommunications Union) regulations. Hence, a current trend in the area of AAs is the design of miniaturized radiating elements that can be grouped into sub-wavelength lattices.

The following formula allows to predict the direction of maximum radiation from the GL in a linear array (similar formulas can be obtained for two-dimensional arrays) [5, Ch. 1]:

$$\theta_{gm} = \sin^{-1}\left(\sin\theta_0 \pm \frac{2m\pi}{k_0 P}\right), m = 1, 2, 3, \ldots \quad (1)$$

where θ_0 is the direction of the main lobe and P is the array periodicity. Thus, the avoidance of the GL within the FoV can be achieved by adjusting appropriately the periodicity of the array lattice. For example, a squared lattice with $P = 0.54\lambda$ allows to steer up to $\pm 50^{\circ}$ all azimuth, while keeping the main beam and the first side-lobe of the GL outside of the FoV. Such an scenario is illustrated in Fig. 1.

Concurrently, during the last years, the interest in designing satellite antennas at higher frequencies has increased, both to produce more compact antennas and to obtain wider bandwidths that allow to achieve higher throughput [1]. Additionally, novel antennas must also be able to operate in dual linear or dual circular polarization (CP).

So far, the most consolidated solution for AAs is based on phased arrays with sub-wavelength radiating patches or apertures embedded in a dielectric medium [6]–[10]. Commercial solutions proposed for LEO [11], [12] or Geostationary Earth Orbit (GEO) [13] AAs are based on this principle. The scanning capabilities of patch-based phased arrays can be further improved thanks to the use of an external radome [14]. Other sub-wavelength antennas, in this case based on dielectric-filled apertures, can be found in [15]–[17].

All previous solutions confirm the classical trend to employ dielectric materials in the conception of electrically small radiating elements. At the same time, avoidance of such materials is also usually preferred in antenna design for space applications and operation in other harsh environments. Multiple factors influence this choice, being limited power

L. Polo-López and M. García-Vigueras are with the Institut d'Electronique et des Technologies du numéRique (IETR), UMR CNRS 6164, INSA Rennes, France e-mail: Lucas.Polo-Lopez@insa-rennes.fr.

E. Menargues and S. Capdevila are with SWISSto12, Renens, Switzerland.

G. Toso is with the Antenna and Sub-Millimeter Wave Section, RF Payloads and Technology Division, European Space Agency ESTEC, Noordwijk, The Netherlands.

This publication is supported by the European Union through the European Regional Development Fund (ERDF), and by the french region of Brittany, Ministry of Higher Education and Research, Rennes Métropole and Conseil Départemental 35, through the CPER Project SOPHIE / STIC & Ondes and also by the region of Brittany under grant SAD volet 1-2019-3Debris.

Manuscript received April 19, 2005; revised August 26, 2015.

This article has been accepted for publication in IEEE Transactions on Antennas and Propagation. This is the author's version which has not been fully edited and content may change prior to final publication. Citation information: DOI 10.1109/TAP.2022.3198512

handling and high insertion losses (which eventually translates into increased power dissipation) the most critical ones. Such limitations have greater impact as the frequency of operation increases. Additionally, their avoidance is even more justified in the context of AAs, due to the DC-to-RF efficiency of solid-state amplifiers in the Ku-band and above, which is still below 50% [18], [19].

Relevant examples of AAs prove the possibility to avoid dielectric materials in front-ends by using all-metal radiating elements. For instance, the DRA on board Eutelsat's Quantum satellite uses full-metal radiating chains of about 3λ periodicity [20], [21]. Other DRA designs with lower periodicity (1.2λ) have been proposed for Medium Earth Orbit (MEO) constellations [22]. Yet, the FoV considered in these proposals is not sufficient to address LEO applications. No sub-wavelength full-metal solution for dual-polarized AAs has been proposed so far in the open literature.

In this context, we propose two original solutions to solve the sub-wavelength lattice reduction in full-metal arrays. The first one is named as mini-horn, it is inspired by [23] and [24], and it is based on a stepped quad-ridge waveguide. Though this design seems the most intuitive way of addressing the problem, it presents some spurious phenomena that degrades its performance.

A second solution that allows to overcome this spurious effect is proposed which is based on evanescent squared apertures (operating below their cutoff frequency). Such elements induce high transmission from quad-ridge waveguides to free space thanks to the use of evanescent mode filters. These Evanescent Quad-ridge Antennas (EQA) enable the design of full-metal AA front-ends with dual polarization capabilities and wide FoV. Here a design methodology for the EQA is presented, as well as a circuit model to explain its performance when operating in a scanning scenario.

Both the innovative EQA and the mini-horn are designed considering the scenario illustrated in Fig. 1, so that their performance can be compared. Due to the theoretical content of this contribution, and the full-metal nature of the antennas, the results are normalized with respect to the central frequency of operation f_0. Nevertheless, the manuscript also includes breadboards in Ku-band to validate experimentally the new concept.

This paper is organised as follows. Section II presents the benchmark and a discussion of its performance. Section III introduces the innovative evanescent antenna and a methodology to synthesize a given bandwidth requirement, while Section IV provides theoretical insight into the modal behaviour of dual-polarized arrays (based on quad-ridge or evanescent apertures) and shows why the proposed approach based on evanescent waveguides provides better performance than alternative designs based on propagating waveguides.

Finally, the performance of a specific EQA design is analysed in Section V, proving the feasibility to scan the main lobe within a FoV of $\pm 50^\circ$ while maintaining a good performance in terms of return loss and cross polarization levels. Additionally, this section also covers the experimental demonstration of the EQA concept. Three prototypes have been built using metallic Additive Manufacturing (AM, based on Selective Laser Melting). The experimental results are discussed together with a tolerance study of the device dimensions, which highlights the robustness of the concept.

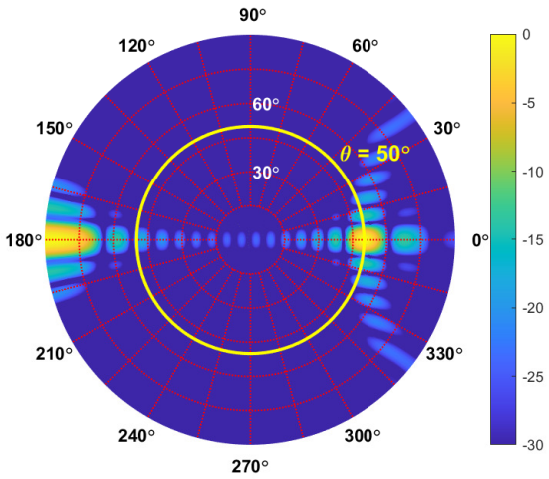


Fig. 1: Array-factor pattern considering a squared lattice of 0.54λ periodicity. The yellow circle corresponds to a FoV of $\pm 50^\circ$. This plot illustrates the scanning of the array main beam at the edge of the FoV, while the first GL remains outside (for an array of 16x16 elements).

II. Array of Quad-Ridge Mini-Horns

The most intuitive solution to reduce the size of the periodic lattice in full-metal arrays is to use mini-horns loaded with ridges. Single and dual-ridge designs with reduced footprint have been proposed in [25]–[27]. The idea of quad-ridge loading to attain sub-wavelength lattice and dual-polarization seems to arise naturally [23], [24]. However, to the authors' best knowledge, it has never been studied before in the open literature.

The proposed quad-ridge mini-horn is represented in Fig. 2. Its input port is sketched in Fig. 2 (c), the dimensions of the four ridges are chosen so that the two degenerate fundamental modes propagate well above the cutoff at the desired operation band. As shown in Fig. 2 (b), this design consists of a stepped transition that expands from the feeding waveguide till an aperture of 0.5λ. Such element can be grouped in an array with a periodicity $P = 0.54\lambda$ (considering a metal thickness between mini-horns of 0.04λ, which corresponds to about $0.5\,\mathrm{mm}$ in Ka-band). This simple design provides an operational bandwidth of 4.5% and dual-linear polarization. Dual-CP can be achieved by adding a polarizer component at its input. The performance of such radiator is analysed next considering the parameters defined in the Appendix.

The performance of the mini-horn is detailed from Fig. 3 to 6, which present respectively the parameters: S_{11}^{Active} defined in (7), S_{21}^{Active} defined in (8), Co-pol defined in (9), and XPD defined in (11). Results are shown for different scanning directions (θ ranging from 0° to 50°) in two significant planes: $\phi = 0^\circ$ and $\phi = 45^\circ$ (these two planes represent the most advantageous scanning scenario, $\phi = 0^\circ$, and the less

This article has been accepted for publication in IEEE Transactions on Antennas and Propagation. This is the author's version which has not been fully edited and content may change prior to final publication. Citation information: DOI 10.1109/TAP.2022.3198512

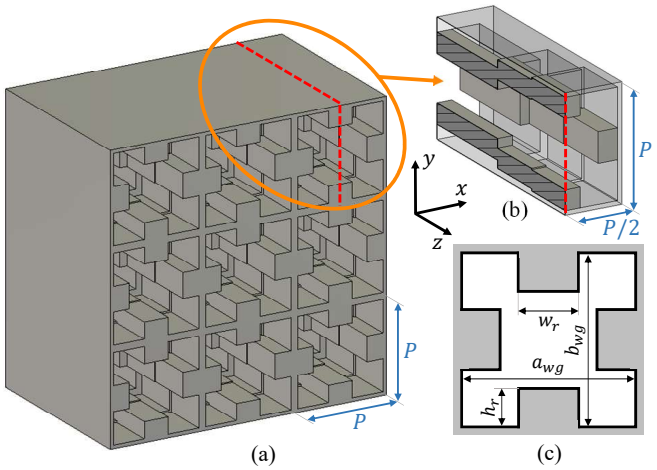


Fig. 2: Structure of proposed mini-horn used as benchmark. (a) Illustration of 3x3 array of elements. (b) Longitudinal inner view of a single element. (c) Quad-ridge input port. $P = 0.54\lambda_0, a_{wg} = b_{wg} = 0.41\lambda_0, w_r = 0.14\lambda_0, h_r = 0.10\lambda_0$.

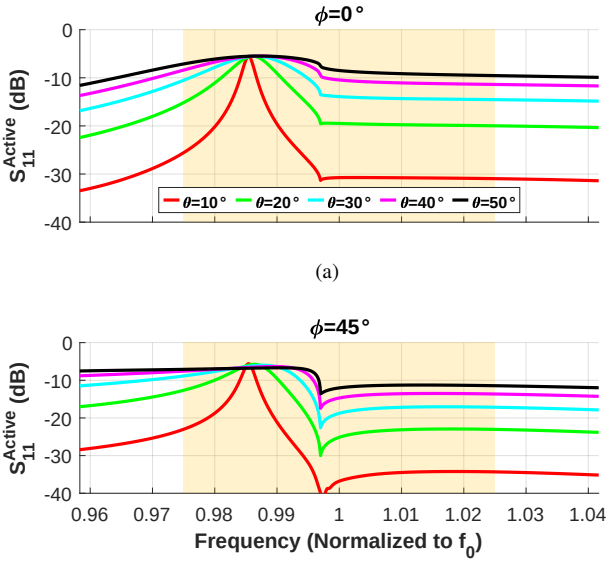


Fig. 3: S_{11}^{Active} of the mini-horn when scanning in different elevation angles θ. Plane (a) $\phi = 0°$ and (b) $\phi = 45°$. For $\theta = 0°$ the values are below $-40\,\mathrm{dB}$; hence, the curves are not shown.

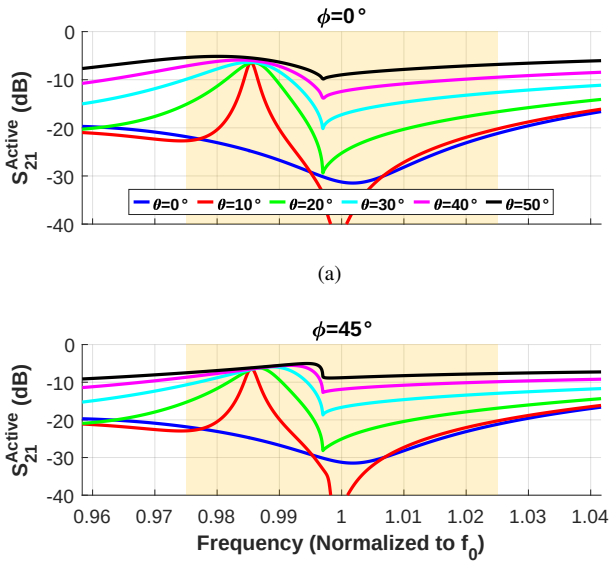


Fig. 4: S_{21}^{Active} of the mini-horn when scanning in different elevation angles θ. Plane (a) $\phi = 0°$ and (b) $\phi = 45°$.

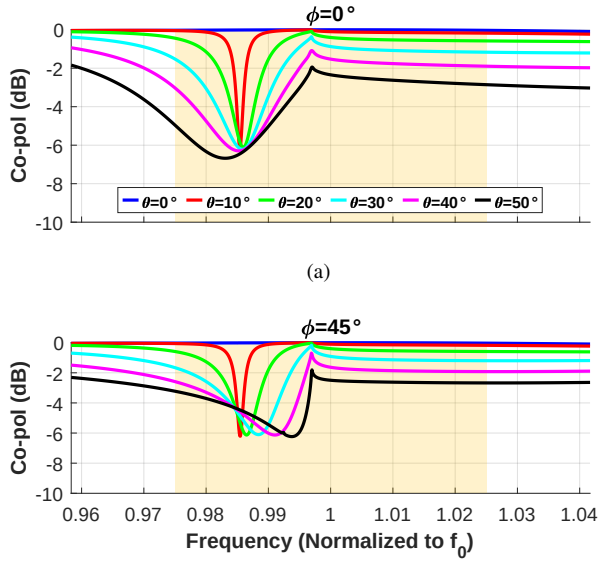


Fig. 5: Co-pol (LHCP) of the mini-horn when scanning in different elevation angles θ. Plane (a) $\phi = 0°$ and (b) $\phi = 45°$.

advantageous scanning scenario, $\phi = 45°$, further explained in Section IV). Note that the results for the plane $\phi = 90°$ are omitted because they are the same as those of $\phi = 0°$. The simulated performance is obtained by simulating the mini-horn in a unit-cell environment (using CST Microwave Studio).

As these figures show, the performance of the mini-horn is very good when pointing at bore-sight (i.e., $\theta = 0°$, $\phi = 0°$). However, as soon as the antenna is scanned, a singular point appears exactly at the frequency $f = 0.997 f_0$, which can be observed in all graphs and for all considered parameters. This frequency value corresponds exactly to the cutoff of the first high order mode of the aperture, which is excited when the dual-symmetry of the mini-horn is broken. This singularity is preceded by a resonance occurring within the frequency band of operation. This spurious resonance spoils the initial good behaviour of the antenna, and the most remarkable consequence is the drastic decrease of the Co-pol levels in Fig. 5, which is associated to the increase of S_{11}^{Active} and S_{21}^{Active} (see Fig.3 and 4). Additionally, the XPD deteriorates significantly in the vicinity of such resonance. The detailed physical explanation for the behaviour of such spurious resonance phenomenon is provided in Section IV.

For the sake of completeness, it should be noted that the design of the mini-horn does not provide freedom to shift the

This article has been accepted for publication in IEEE Transactions on Antennas and Propagation. This is the author's version which has not been fully edited and content may change prior to final publication. Citation information: DOI 10.1109/TAP.2022.3198512

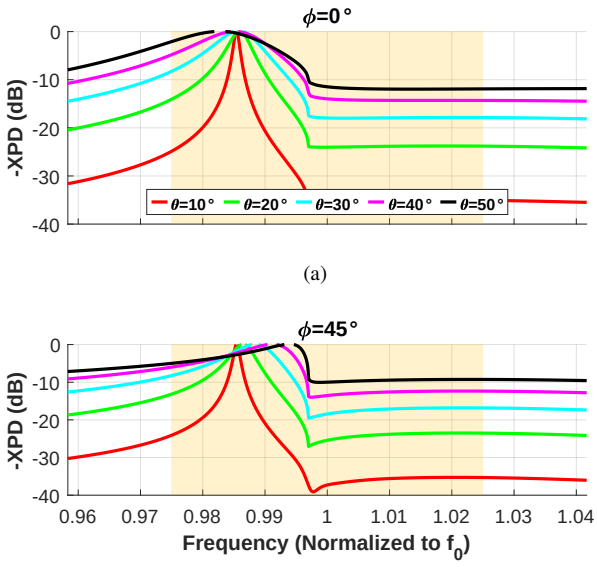


Fig. 6: XPD of the mini-horn when scanning in different elevation angles θ. Plane (a) $\phi = 0°$ and (b) $\phi = 45°$. For $\theta = 0°$ the values are below $-40\,\mathrm{dB}$; hence, the curves are not shown.

appearance of the spurious resonance away from the operation band [23]. On the one hand, the antenna design imposes that the ridges should be sufficiently large so that the cutoff frequency of the fundamental degenerate modes is below the operation band. Once this dimension is chosen to operate at a given frequency, the cutoff frequency of the high order mode is also determined and therefore it cannot be modified by optimizing the geometry of the waveguide. The mono-modal frequency band of quad-ridge waveguides is inherently very narrow [23]. Moreover, as it has been seen in the graphs above, the spurious resonance associated to the first high order mode appears below its cutoff frequency.

On the other hand, operating above the launching of the high order mode (e.g. choosing as operation band the range from f_0 to $1.04f_0$) and accepting its excitation is not an interesting option because this high order mode drains power from the fundamental mode, which produces an increment of the scan loss, reducing therefore the antenna efficiency. In fact, the mini-horn presents relatively high scan losses (almost $3\,\mathrm{dB}$ when scanning to the FoV) even at these frequencies. In addition, regardless of the scan loss, the maximum operation frequency is limited by the appearance of GLs. As illustrated in Fig. 1, the array periodicity has been chosen so that the GL remains outside of the FoV when the main beam is scanned to its edge. By operating at higher frequencies the periodicity would be increased (in electrical terms) and therefore the GL would get into the FoV.

In conclusion, according to these results, the mini-horn presents important limitations when used in a steering scenario. Depending on the application requirements, these limitations might be acceptable and the mini-horn would then constitute an adequate solution. Nevertheless, in order to also

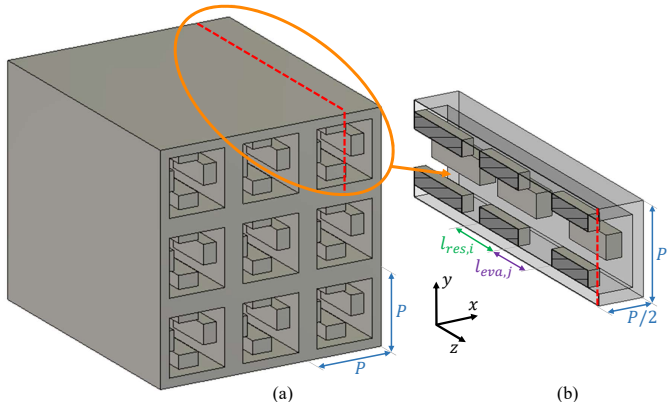


Fig. 7: Structure of proposed EQA for the case of $N = 2$. (a) Illustration of 3x3 array of elements. (b) Inner view of a single element. In this example, the input port is equal to the one in Fig. 2 (c), the aperture size is $0.41\lambda_0$ and $P = 0.54\lambda_0$.

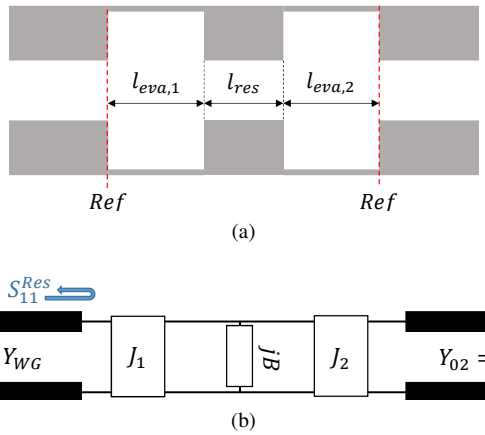


Fig. 8: (a) Schematic representation (lateral view) of a quad-ridge resonator with two adjacent evanescent waveguide sections that act as admittance inverters. The reference planes for the S-parameters calculation are marked by dashed red lines. (b) Circuit equivalent of this structure.

give response to application cases where a higher performance is required, the next section presents a more sophisticated quadridge aperture concept that overcomes the limitations seen in the mini-horn design.

III. Evanescent Quad-ridge Antenna

A. Antenna description and design process

In this section we present the evanescent quad-ridge antenna (EQA) as a successful alternative to induce radiation from sub-wavelength apertures. The possibility to induce high transmission through evanescent apertures has been demonstrated in the context of periodic metal screens [28], and for interleaved and overlapped GEO subarrays [29]. In this last reference, the antenna is not used for scanning purposes, and the case of single-ridge, single-polarized waveguides is considered.

The proposed EQA is represented in Fig. 7. As in the case of the mini-horn, a quad-ridge waveguide is used at the feeding port to enable dual-mode excitation and dual-polarized

This article has been accepted for publication in IEEE Transactions on Antennas and Propagation. This is the author's version which has not been fully edited and content may change prior to final publication. Citation information: DOI 10.1109/TAP.2022.3198512

radiation from the antenna. However, in this concept, instead of gradually opening the waveguide to induce transmission, the EQA uses cascaded sections of evanescent squared waveguide and propagating quad-ridge waveguide (of respective length $l_{eva,j}$ and $l_{res,i}$) with constant dimensions along the longitudinal axis (z in Fig. 7). These waveguide sections allow to couple the energy from the input port to the free-space.

The proposed EQA design methodology is based on the slope-parameter filter technique presented in [29], [30]. The evanescent waveguides are regarded as inverters, and the quad-ridge sections as resonators. In the present case, for the iterative refinement of the resonators' susceptance, the equivalent circuit in Fig. 8 applies, and it results in the following equation [31]:

$$S_{11}^{Res} = \frac{J_2^2 Y_{01}^* - J_1^2 Y_{02} + jBY_{01}^* Y_{02}}{J_2^2 Y_{01} + J_1^2 Y_{02} + jBY_{01} Y_{02}}, \quad (2)$$

where J_1 and J_2 are the admittance inverter values of the two evanescent waveguide sections adjacent to a certain quad-ridge resonator, and $Y_{01} = Y_{02} = Y_{WG}$ is the wave admittance of the quad-ridge waveguide fundamental mode. By means of a full-wave simulation the value of S_{11}^{Res} can be obtained, which allows to determine the new estimated value of the resonator susceptance (B).

It should be noted that the EQA can be modelled by adopting conventional theory of evanescent filters [32, Ch. 4]. Although it is out of the scope of the present contribution, it is expected that the design of EQAs can also consider selectivity criteria, extended harmonic rejection, enhancement of the power handling, etc.

B. Bandwidth control

Similarly to conventional filters, the bandwidth of EQA can be determined by the number of resonators used in its design. In general, increasing the number of resonators (i.e., the order, N) permits to obtain a design with wider bandwidth. To illustrate this, Fig. 9 presents three different designs with $N = 2, 4$ and 6. It should be clarified that there is a practical limitation in the maximum bandwidth achievable by the EQA. It has been found that the limiting factor is the length of the last evanescent section (i.e. the one that interfaces between guiding media and free space). When increasing the bandwidth of EQA, the value of the admittance inverters associated to each evanescent section increases. Nevertheless, the required admittance inverter value of the last evanescent section increases faster than those corresponding to internal sections. Since greater inverter values are synthesized by means of shorter evanescent sections, there is a manufacturing limitation related to the greatest inverter value that can be synthesized.

Table I lists the admittance inverter value of the last evanescent section, J_{last} (such values are normalized to the wave admittance of the quad-ridge waveguide fundamental mode), for the three examples in Fig. 9. These three values remain below the value 0.984, which has been chosen as a limit corresponding to $30\,\mu\text{m}$ ($\pm 10\,\mu\text{m}$ due to tolerances) at a typical operation frequency of $f_0 = 24\,\text{GHz}$. These figures correspond to the smallest feature that could be manufactured using classical machining or metal 3D printing. Please note

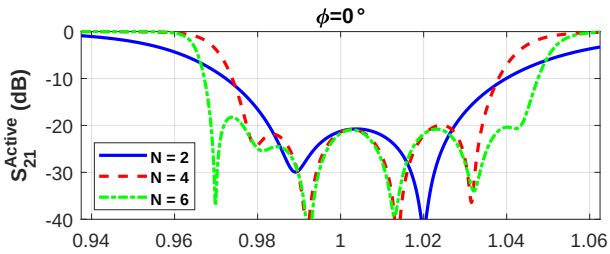


Fig. 9: S_{21}^{Active} for three EQA with different order.

TABLE I: Bandwidth and J_{last} for three EQA with different order.

	N = 2	**N = 4**	**N = 6**
ΔBW	4.5%	5.7%	7.5%
J_{last}/Y_0	0.940	0.913	0.983

that this choice of f_0 is completely arbitrary and just follows an illustrative purpose. The same reasoning could be followed for any other frequency value.

Additionally, it should be noted that for the adequate functioning of the filter it is necessary that the operation bandwidth is above the cutoff frequency of the ridge sections and below the cutoff frequency of the evanescent sections. This same limitation appears in conventional filters where several resonating cavities are coupled through irises.

Consequently, following the previous design methodology, the widest fractional bandwidth that has been attained with the EQA is 7.5%. Further increase could be achieved by adopting full-wave optimizations and using this design as starting point. It should be noted that such constraint does not fully limit the antenna applicability, since these fractional bandwidths are typically sufficient for multiple use cases of AAs with wide FoV (e.g., military Ka-band in downlink and uplink is 5% and 3.5% respectively, while commercial Ku-band uplink is less than 6%).

IV. Dual-polarized discontinuities and spurious mode excitation

The dual-polarized discontinuities considered in the mini-horn and the EQA are here analysed from a physical insightful perspective. This allows to understand ans justify the eventual appearance of spurious phenomena.

A. Modal solutions in radiating apertures

The antenna radiating aperture is a square quad-ridge discontinuity in the case of the mini-horn, and an empty squared discontinuity in the case of the EQA. The first three modal solutions of both of these apertures are analysed with CST, and their field profile and cutoff frequencies (f_c^{Mi}) are depicted in Fig. 10. The first two modes (M1 and M2) are the fundamental ones, and they are degenerate (i.e. they have the same cutoff frequency, and their field distribution is equal with a $90°$ rotation). In the case of the quad-ridge aperture, all modes start propagating earlier than for the evanescent one, due to the influence of the ridges. As it can be seen in Fig. 10, the

This article has been accepted for publication in IEEE Transactions on Antennas and Propagation. This is the author's version which has not been fully edited and content may change prior to final publication. Citation information: DOI 10.1109/TAP.2022.3198512

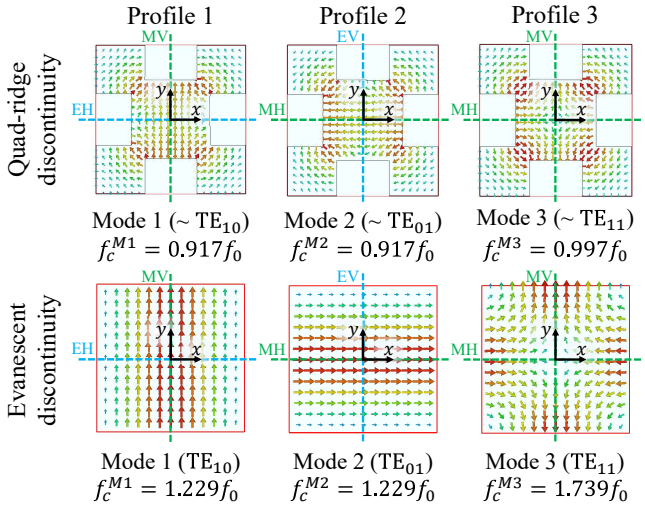


Fig. 10: Three first modal solutions in quad-ridge and evanescent apertures. The electric field patterns are represented, and the electric (E) and magnetic (M) symmetries appearing in vertical (V) or horizontal (H) axes are highlighted.

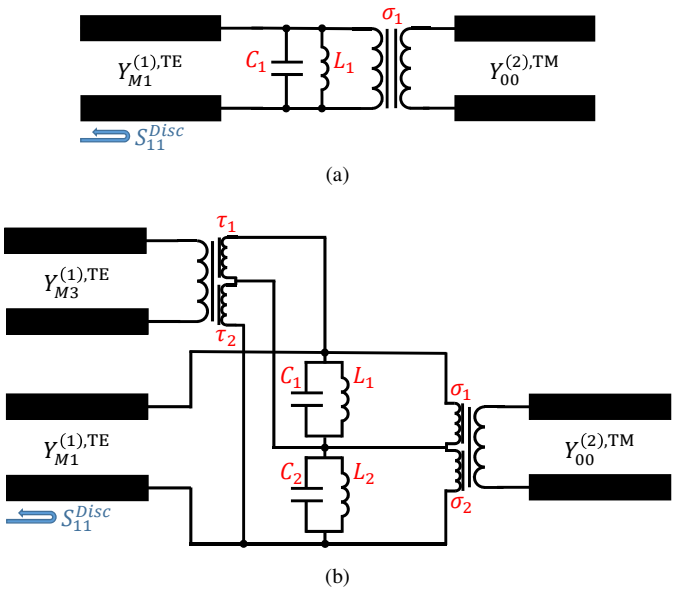


Fig. 11: Circuits to model the discontinuity between the antenna aperture and the free space under M1 excitation. (a) Circuit 1: Simplest circuit assuming no coupling between waveguide modes. (b) Circuit 2: Extension to consider eventual coupling of M3.

field distributions of these three modes are somehow similar in both apertures. They correspond to the TE_{10}, TE_{01} and TE_{11} modes of the squared waveguide, and they are perturbed by the ridges in the case of the quad-ridge discontinuity.

The aperture of the array can be regarded as a periodic discontinuity between the guided medium and free-space (which implies the consideration of an array of infinite elements). At this interface there is an exchange of power between the waveguide modes and the free space modal solutions, which are TE- and TM-polarized plane waves. This coupling between the different modes is carried out through different aperture field profiles, which present the same transverse field distribution as the aforementioned waveguide modes. For example, below the appearance of GLs, and when scanning in the $\phi = 90°$-plane, M1 couples to a TM-polarized plane-wave radiating in free space (the fundamental TM_{00} harmonic) through the Profile 1. In the same circumstances, the guided M2 couples to the fundamental TE_{00} harmonic through the Profile 2, and M3 to the TM_{00} harmonic through the Profile 3. Note that each Floquet harmonic is denoted with its variation order mn, as it is done in [28]. Therefore, the fundamental ones are referred to as 00.

The considered dual-polarized apertures are symmetric with respect to the horizontal ($y = 0$) and vertical ($x = 0$) planes, as it can be seen in Fig. 10. In particular, M1 presents electric-horizontal and magnetic-vertical symmetries, while the ones presented by M2 are magnetic-horizontal and electric-vertical. Finally, M3 presents magnetic-horizontal and magnetic-vertical symmetries. These symmetry conditions imply that, when all the elements of the array are excited in phase (i.e. when pointing at bore-sight), the modes orthogonality is respected and there is no transfer of energy between them. However, when the symmetry of the structure is broken or as soon as the beam is steered, coupling between modes may occur. For example, M1 and M3 will couple when scanning in the $\phi = 90°$-plane, and M2 with M3 in the $\phi = 0°$-plane. When steering the beam out of the main planes, M1 and M2 will also couple (specially when $\phi = 45°$).

B. Circuit modelling of the aperture

The circuits depicted in Fig. 11 model the periodic discontinuity between the last waveguide section of the antenna array and free-space. For the sake of simplicity, the structure is considered to be fed by the M1 (vertical excitation). The case of M2 excitation can be considered analogously. The modal-expansion approach proposed in [28], [33]–[35] is adopted. The medium to the left of the discontinuity is guided whereas the medium to the right is free-space, and they are respectively denoted by the superscripts (1) and (2).

On the one hand, the simple circuit of Fig. 11 (a) characterizes the active S parameters assuming no coupling between waveguide modes [33]. The transmission line with characteristic admittance $Y_{M1}^{(1),\mathrm{TE}}$ represents the propagation of M1 in the last waveguide section of the antenna. As it is justified above, this mode couples to the fundamental TM-harmonic in free-space, which is modeled by the transmission line with admittance $Y_{00}^{(2),\mathrm{TM}}$. The degree of excitation of such wave is accounted for by the transformer of ratio σ_1. Finally, the terms C_1, L_1 account for the quasi-static excitation of all high order modal solutions that are compatible with M1 at both sides of the discontinuity. In particular, C_1 and L_1 represent modes of TM and TE nature, respectively. Since the periodicity of the array is sub-wavelength, no GL is expected to propagate at the frequency of operation, and such quasi-static approximation is valid [33].

On the other hand, the extended version of the circuit presented in Fig. 11 (b) captures the possible excitation of

This article has been accepted for publication in IEEE Transactions on Antennas and Propagation. This is the author's version which has not been fully edited and content may change prior to final publication. Citation information: DOI 10.1109/TAP.2022.3198512

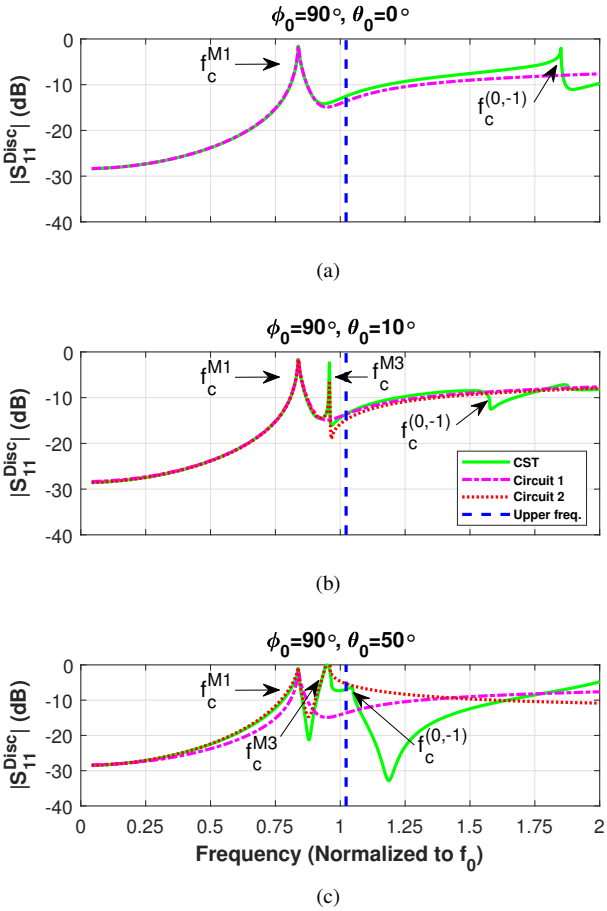


Fig. 12: Active reflection coefficient of a periodic discontinuity of quad-ridge square apertures. Comparison between full-wave simulations (CST) and the circuit models in Fig. 11.

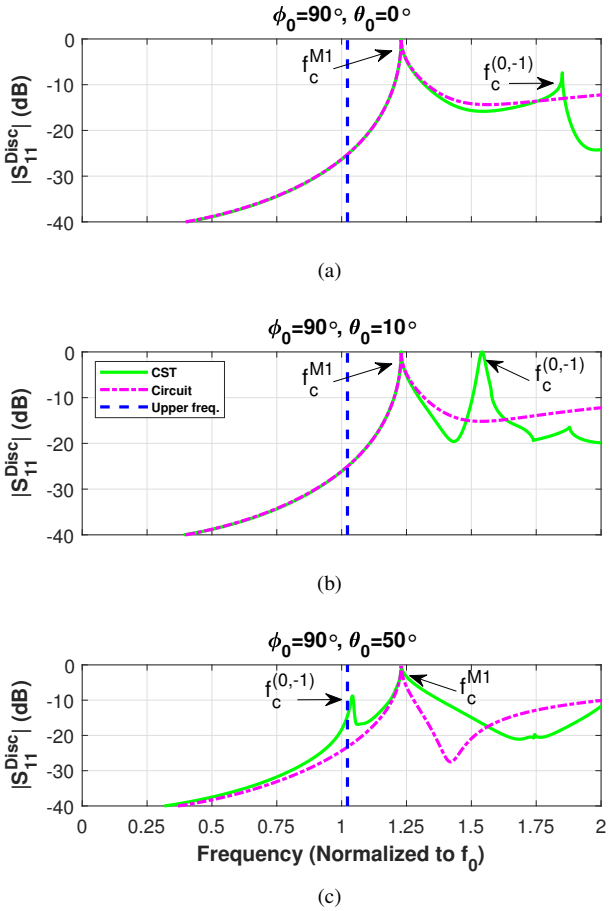


Fig. 13: Active reflection coefficient of a periodic discontinuity of square evanescent apertures. Comparison between full-wave simulations (CST) and the circuit model in Fig. 11 (a).

M3. Such scenario implies a considerable increase of the circuit complexity. As it is discussed in [28], [34], [35], this extension is typically needed when characterizing dual-polarized apertures illuminated under oblique incidence, and it involves the consideration of two different field profiles in the discontinuity (profile 1 and profile 3). As explained in those references, the energy coupling is characterized explicitly through the transformers τ_1 and τ_2. Though analytical models could be derived based on previous references, the circuit in Fig. 11 (b) is a simplified version of the ones proposed in [28], [34], [35], with the difference that the mutual couplings between high order modes are not characterized to simplify the numeric fitting. Such simplification implies a decrease of the accuracy, which in our case can be accepted since the purpose of the circuit is to capture the main singular effects and provide physical explanations to them.

The value of the admittances in the circuits of Fig. 11 can be computed from:

$$Y_{Mi}^{(1),\mathrm{TE}} = -\mathrm{j}k_{z,Mi}/(\omega\mu_0), \tag{3}$$

$$Y_{00}^{(2),\mathrm{TM}} = \mathrm{j}\omega\varepsilon_0/k_{z,00}, \tag{4}$$

where:

$$k_{z,Mi} = \begin{cases} \beta_{Mi} = k_0\sqrt{1-f_c^{Mi}}, & \text{if } f \geq f_c^{Mi} \\ -\mathrm{j}\alpha_{Mi} = -\mathrm{j}k_0\sqrt{f_c^{Mi}-1}, & \text{if } f < f_c^{Mi} \end{cases} \tag{5}$$

is the propagation constant of the mode Mi, $k_{z,00} = k_0 sin(\theta)$ is the propagation constant of the TM fundamental harmonic and $k_0 = 2\pi f/c$ is the free-space wave-number. The value of the unknowns in the circuits (namely, the inductors, capacitors and transformer ratios) can be obtained by numerical fitting with full-wave simulations.

The two considered discontinuities are next analysed, comparing full-wave simulations and circuit responses. As it will be shown, the circuital results allow to have a better comprehension of the phenomena observed in the full-wave simulations. In Fig. 12 the quad-ridge aperture (associated to the mini-horn design) is considered, and the evanescent one (EQA design) is studied in Fig. 13. It can be observed that Circuit 1 performs well for the quad-ridge aperture only when the beam is not scanned. In this scenario (Fig. 12 (a)) the circuit predictions match with accuracy the full-wave response. The first peak of $S_{11}^{Disc} = 1$, appearing below f_0, is well captured by Circuit 1 in all cases depicted in Fig. 12. This peak is associated to the transition evanescent-to-propagating

This article has been accepted for publication in IEEE Transactions on Antennas and Propagation. This is the author's version which has not been fully edited and content may change prior to final publication. Citation information: DOI 10.1109/TAP.2022.3198512

of M1, since $Y_{M1}^{(1),\mathrm{TE}} = 0$ at f_c^{M1}. Nevertheless, even for small elevation angles, an additional resonance appears below f_0 which is not grasped by Circuit 1. This peak is related to the excitation of M3 in the quad-ridge waveguide, and it is well predicted by Circuit 2. The coupling to M3 results in two remarkable phenomena: a singular point of minimum reflection appears at f_c^{M3} (where $Y_{M3}^{(1),\mathrm{TE}} = 0$), that is preceded by a peak of full reflection (which is related to the fact that $Z_{M3}^{(1),\mathrm{TE}} = 1/Y_{M3}^{(1),\mathrm{TE}}$ tends to infinity, meeting somewhere an inductive value that causes a resonance in series, and thus, a short-circuit). In Figs. 3 to 6, such dual-behaviour can also be clearly identified, since the singular point appears always at f_c^{M3}, and it is preceded by a resonance. Therefore, the proposed circuit provides a theoretical basis that explains the glitch observed in these figures. This behaviour was firstly explained in terms of equivalent circuits in [33].

Finally, it should be noted that a third resonance appears above f_0 in Fig. 12, which shifts down in frequency while the scanning angle increases. Such peak is related to the launching of the first GL (the $\mathrm{TM}_{0,-1}$ Floquet harmonic). Neither of the circuits grasp the effect of this mode, since its contribution is not explicitly considered and it has been modelled along with the other harmonics in the LC resonators. When the beam is steered, the cutoff of the harmonic $f_c^{(0,-1)}$ approaches f_0, and therefore the quasi-static approximation becomes less accurate. However, it can be appreciated that for all the scanning directions this peak is above the operation band (marked by the dashed blue line in the figures). This confirms the accurate choice of P made in Fig. 1.

For the case of the evanescent squared aperture considered in Fig. 13, it can be observed that Circuit 1 matches the full-wave response with great accuracy for all scanning angles, since this aperture does not present a high order mode that is being excited in the operation frequency band. In analogy to the previous case, the peak of $S_{11}^{Disc} = 1$ appearing at $f_c^{M1} = 1.23 f_0$ corresponds to the transition evanescent-to-propagating of M1, which appears above f_0 in this case since the aperture is evanescent. Additionally, the effect of the Floquet harmonic $\mathrm{TM}_{0,-1}$ is also observed at the same frequencies as before; which is again not reproduced by the circuit for the same reasons.

Lastly, thanks to the proposed circuit models it can be concluded that the spurious resonance appearing in the performance of the mini-horn is produced by the first high order mode of the quad-ridge waveguide (mode 3). The EQA design is free from this effect since, thanks to the use of an evanescent discontinuity that already operates below the cutoff of the fundamental mode, keeps the first high order mode very far from the operation band.

V. EQA Performance Validation

A. Simulated performance

An illustrative example of EQA with N = 2 is analysed in this section to illustrate the AA performance. The periodicity and the operational bandwidth are 0.54λ and 4.5% respectively, as in the mini-horn benchmark. Other dimensions of the EQA are: $l_{eva,j}/\lambda_0 = (0.11, 0.20, 0.02)$ and $l_{res,i}/\lambda_0 = (0.45, 0.30)$. The simulations are again performed in periodic environment, and the performance parameters are those that have been used before and described in the Appendix.

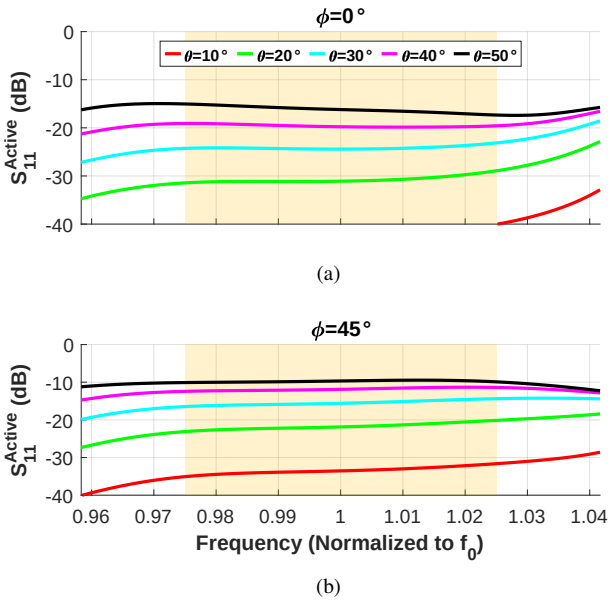


Fig. 14: S_{11}^{Active} of the EQA when scanning in different elevation angles θ. Plane (a) $\phi = 0°$ and (b) $\phi = 45°$. For $\theta = 0°$ the values are below $-40\,\mathrm{dB}$; hence, the curves are not shown.

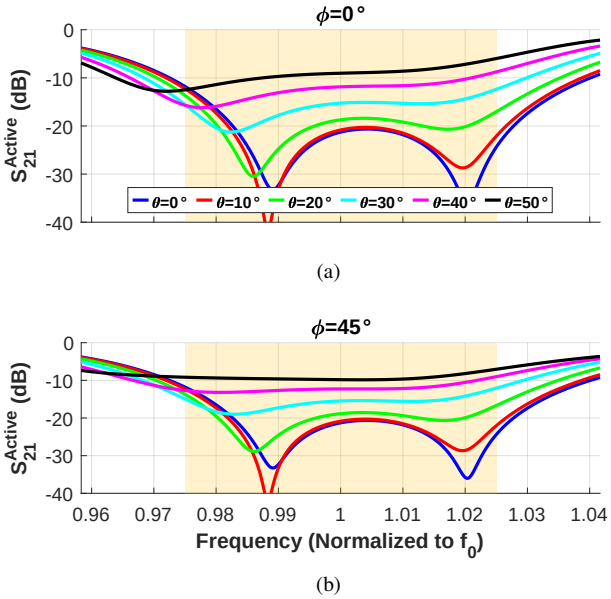


Fig. 15: S_{21}^{Active} of the EQA when scanning in different elevation angles θ. Plane (a) $\phi = 0°$ and (b) $\phi = 45°$.

The performance of the EQA is detailed in Fig. 14 to 17, which consider respectively the parameters: S_{11}^{Active}, S_{21}^{Active}, Co-pol, and XPD. Results are also shown for different scanning directions (θ ranging from $0°$ to $50°$) in two significant planes: $\phi = 0°$ and $\phi = 45°$. As before, the results for the plane $\phi = 90°$ are omitted.

The performance of the EQA is very good when scanning

This article has been accepted for publication in IEEE Transactions on Antennas and Propagation. This is the author's version which has not been fully edited and content may change prior to final publication. Citation information: DOI 10.1109/TAP.2022.3198512

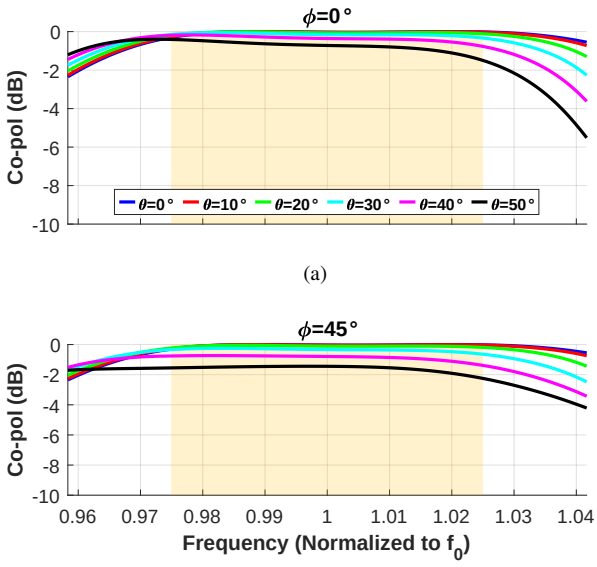


Fig. 16: Co-pol (LHCP) of the EQA when scanning in different elevation angles θ. Plane (a) $\phi = 0°$ and (b) $\phi = 45°$.

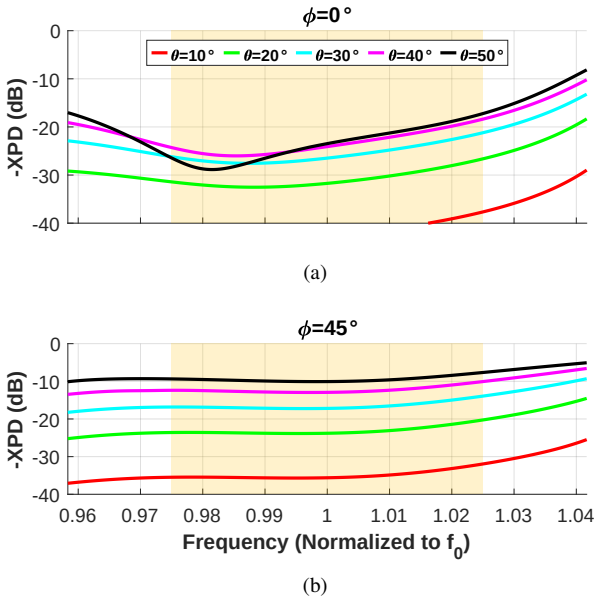


Fig. 17: XPD of the EQA when scanning in different elevation angles θ. Plane (a) $\phi = 0°$ and (b) $\phi = 45°$. For $\theta = 0°$ the values are below $-40\,\mathrm{dB}$; hence, the curves are not shown.

anywhere within the FoV. Both S_{11}^{Active} and S_{21}^{Active} remain below $-20\,\mathrm{dB}$ in the bore-sight direction and gradually deteriorate up to around $-10\,\mathrm{dB}$ as the elevation angle increases (which is considered as an industry standard for active reflection coefficient). In terms of Co-pol, the levels of insertion loss stay below $2\,\mathrm{dB}$ in all the bandwidth and the FoV, as shown in Fig. 16. Finally, the XPD in the plane $\phi = 0°$ is excellent, remaining always better than $20\,\mathrm{dB}$. Results are slightly worse in the plane $\phi = 45°$, decreasing from $35\,\mathrm{dB}$ to $10\,\mathrm{dB}$ as the elevation angle increases. Nevertheless, this is still a remarkable result, since this is typically the most

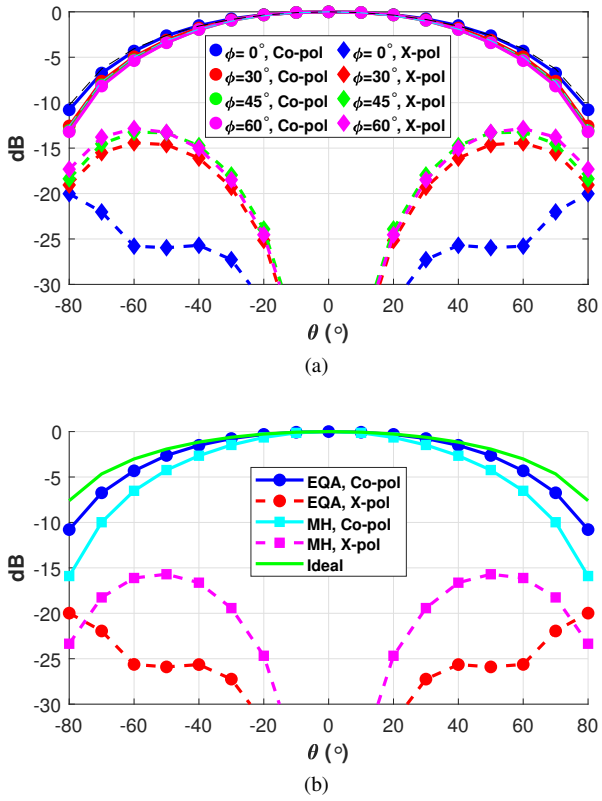


Fig. 18: (a) EQA normalized embedded radiation pattern at f_0. (b) EQA and mini-horn (MH) normalized embedded radiation pattern ($\phi = 0°$) at f_0. In both cases, directivity: $5.62\,\mathrm{dBi}$.

challenging scanning scenario (see Section IV). Moreover, in contrast to the mini-horn, the EQA does not suffer from any spurious resonance within its operational bandwidth. This advantage is justified in Section IV. Additionally, since the S_{21}^{Active} is around -10 dB or better in all the bandwidth and the FoV, the EQA can be used in dual-CP operation without any restriction.

The EQA embedded radiation pattern for f_0 is shown in Fig. 18 (a). The simulated bore-sight directivity is $5.6\,\mathrm{dBi}$. The plane $\phi = 0°$ exhibits scan loss following $\cos^{1.35}\theta$, while the plane $\phi = 45°$ exhibits scan loss following $\cos^{1.65}\theta$. In addition, Fig. 18 (b) compares the embedded radiation pattern of the EQA with that of the mini-horn. The green line corresponds to a scan loss of $\cos\theta$, which is the minimum attainable scan loss. As it can be seen, the EQA is significantly closer to this ideal bound, whereas the mini-horn presents a scan loss following $\cos^{2.10}\theta$. This is explained by the fact that the EQA array does not excite the high order mode of the quad-ridge waveguide when the radiation pattern is steered; hence, no power is deviated to other spatial directions as it occurs with the mini-horn. Alternatively, both designs can be compared more clearly by directly studying how their scan losses or aperture efficiencies vary with the scanning direction. These two parameters are represented in Fig. 19. Again, it can be observed that the EQA outperforms the mini-horn under oblique incidence.

For the sake of completeness, a case considering an array

This article has been accepted for publication in IEEE Transactions on Antennas and Propagation. This is the author's version which has not been fully edited and content may change prior to final publication. Citation information: DOI 10.1109/TAP.2022.3198512

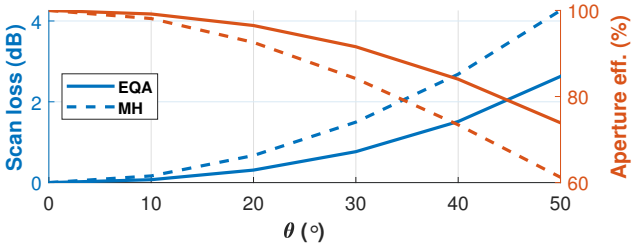
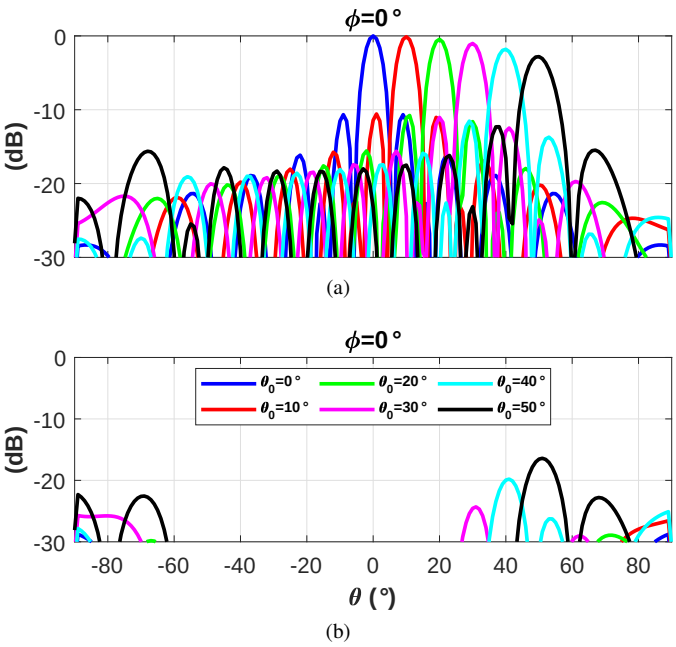


Fig. 19: Scan loss and aperture efficiency of the EQA and mini-horn (MH) at f_0 for different scanning directions in the plane $\phi = 0°$.



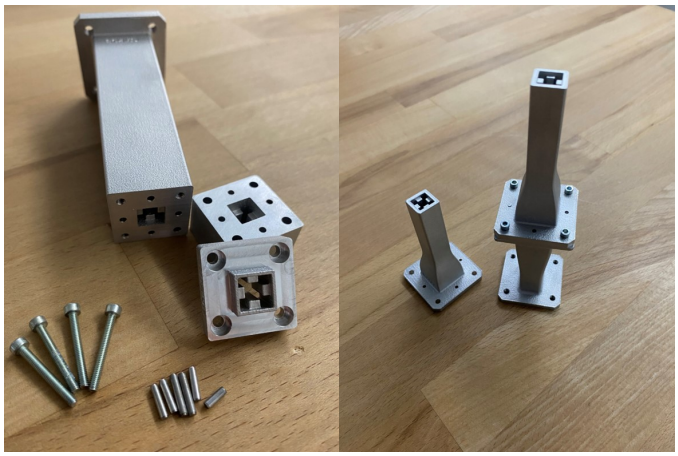
(a)

(b)

Fig. 20: Normalized radiation pattern produced by an array of 16x16 EQAs for different scanning angles in elevation along the plane $\phi = 0°$. All the patterns are normalized to the peak in bore-sight (realized gain: $24.08\,\mathrm{dBi}$). (a) Co-pol. (b) X-pol.

of 16x16-elements is also included in the article. These results have been obtained by combining the performance of the unit-cell with the corresponding array factor, and this permits generalizing and validating the results. The choice of the array size is arbitrary, and the radiation pattern results could have been obtained for different array configurations by using the corresponding array factor. Fig. 20 shows Co-pol and X-pol when scanning in elevation along the plane $\phi = 0°$.

Despite the previous example has been discussed assuming a normalized frequency and perfect electric conductor, it is worth evaluating the insertion loss of the antenna and its dependency with frequency. Three examples at $12\,\mathrm{GHz}$, $24\,\mathrm{GHz}$ and $48\,\mathrm{GHz}$ have been considered (lower frequencies are not evaluated, since the EQA would be physically too large, thus being less interesting for flat arrays). The study assumes a conductivity of $3.56 \times 10^7\,\mathrm{S\,m^{-1}}$ (conductivity of the Aluminium). The obtained loss values for each of these cases are $0.08\,\mathrm{dB}$, $0.10\,\mathrm{dB}$ and $0.14\,\mathrm{dB}$, respectively. These values correspond to a radiation efficiency of 98.3%, 97.7% and 96.8%, respectively. Further comparison with other state-of-the-art devices is provided in Section V-C.



(a) (b)

Fig. 21: Photographs of the experimental demonstrators (a) EQA#1 and (b) EQA#2.

TABLE II: Dimensions (in mm) of the experimental demonstrator.

a_{wg}	h_{rid}	w_{rid}	$l_{res,1}$	$l_{res,2}$	$l_{eva,1}$	$l_{eva,2}$	$l_{eva,3}$
8.56	2.00	2.95	9.24	5.94	2.52	4.24	1.32

B. Experimental Demonstrator

In order to demonstrate the feasibility of the new component, three demonstrators have been manufactured and characterized experimentally. The prototypes are shown in Fig. 21. The order of the EQAs is $N = 2$ and the bandwidth of operation is approximately 14-14.5 GHz (3.5% with a central frequency of $14.25\,\mathrm{GHz}$, corresponding to the uplink in Ku-band). Despite the lack of neighbouring apertures the followed design procedure is the same described in Section III-A. The dimensions of this device are summarized in Table II.

The three prototypes correspond to two different versions of the previous EQA. The fabrication technique used in all cases is metallic AM. The first version (EQA#1, see Fig. 21 (a) and Fig. 22 (a)) is divided in three blocks, each one containing a resonator and a coupling iris. The second version (EQA#2, see Fig. 21 (b) and Fig. 22 (b)) has been built following a monolithic approach (i.e. in a single part). This requires to make certain modifications to the ridges in order to enable vertical 3D printing [36]. For this second design, two identical prototypes have been manufactured to assess their repeatability.

Both EQA#1 and EQA#2 are excited by means of a rectangular to quad-ridge transition. The internal air volume of this device is depicted in Fig. 22 (c). Since the width of the transition is greater than that of the quadridge waveguide, it may arise the question on whether a $0.54\lambda_0$ periodicity could be achieved for a complete array. Nevertheless, this can be perfectly addressed by using meandered waveguides as an interface between the transitions and the EQAs [37].

This article has been accepted for publication in IEEE Transactions on Antennas and Propagation. This is the author's version which has not been fully edited and content may change prior to final publication. Citation information: DOI 10.1109/TAP.2022.3198512

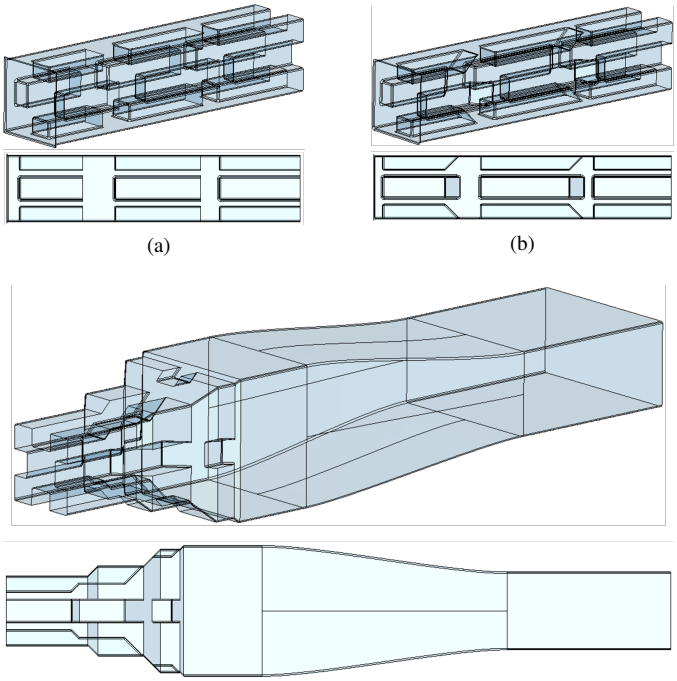


Fig. 22: Internal air volumes (perspective and lateral view) of the experimental demonstrators: (a) EQA#1, (b) EQA#2, (c) rectangular to quad-ridge transition.

The transition has been fabricated as a separated part so it can be rotated $90°$ in order to excite both the vertical and the horizontal polarizations. In a real application, the device would typically be excited through a ridged polarizer [38], a miniaturized OMT or coaxial launchers fed in sequential rotation.

The measured and simulated return losses are shown in Fig. 23 (a)-(b). A value better than $20\,\mathrm{dB}$ is obtained in the operation bandwidth, which is an excellent result for a sub-wavelength aperture. Moreover, it should be highlighted that this return loss level is achieved simultaneously for both polarizations. In fact, the response for the two polarizations is almost identical, showing that the manufacturing process respects the symmetry of the design. Additionally, the high degree of agreement for the measurements of both EQA#2 prototypes demonstrates the repeatability achievable using metallic AM.

Figure 23 (c) illustrates the measured realized gain for both prototypes compared with the simulated values. The excellent agreement between both sets of results demonstrates the feasibility of the EQA as a viable radiating element.

The measured XPD is represented in Fig. 23 (d). It should be noted that the simulated XPD is not depicted since, due to the symmetries of the structure, its value is infinite. As it can be observed the measured XPD is better than $20\,\mathrm{dB}$ for both EQA#1 and EQA#2, which can be considered as a good result, specially taking into account the experimental character of the employed manufacturing technique.

Finally, Fig. 24 shows the measured radiation pattern for

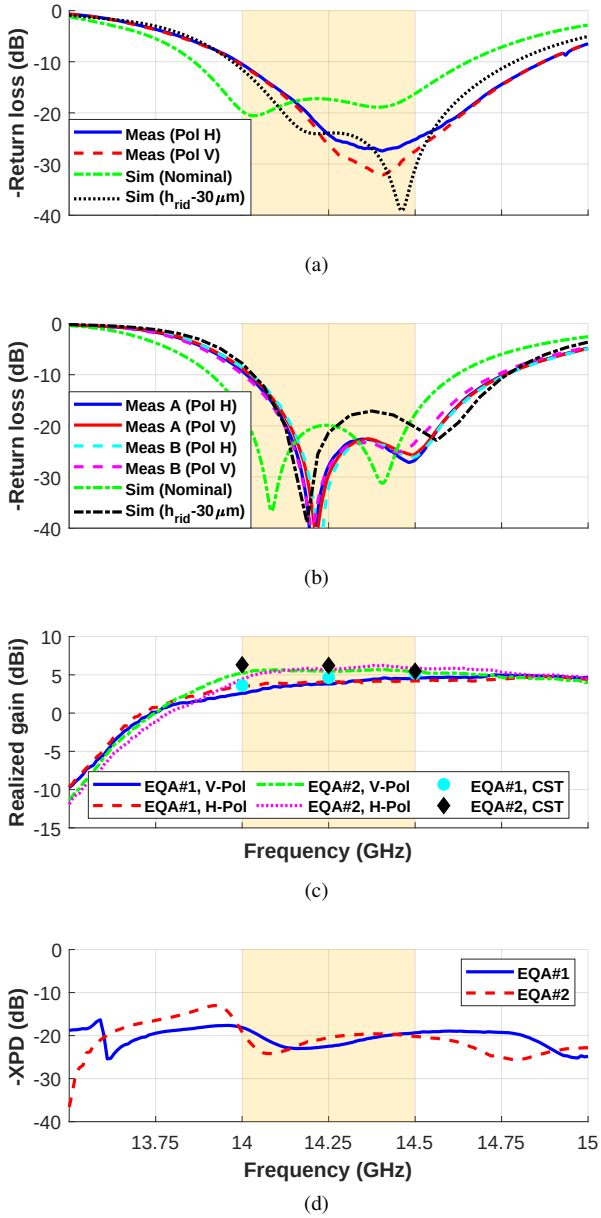


Fig. 23: Measured return loss for (a) EQA#1 and (b) EQA#2 (A and B make reference to each of the manufactured copies). Measured (c) realized gain and (d) XPD for both demonstrators.

both prototypes. As it can be seen there is an excellent agreement with the simulations not only on the copolar but also on the cross-polarized component in the diagonal plane. Moreover, the XPD in the main planes ($\phi = 0°, \phi = 90°$) is better than $25\,\mathrm{dB}$ for all the elevation angles.

As it can be appreciated in Fig. 23 (a)-(b), there is a small shift of the measurements towards higher frequencies with respect to the simulations which corresponds with a $30\,\mu\mathrm{m}$ deviation of h_r. This deviation is in the range of tolerances inherent to the manufacturing process. A study has been made to check how do these tolerances affect to each design parameter. As it can be seen in Fig. 25, the EQA is very robust except for alterations of h_r. However, since this error

This article has been accepted for publication in IEEE Transactions on Antennas and Propagation. This is the author's version which has not been fully edited and content may change prior to final publication. Citation information: DOI 10.1109/TAP.2022.3198512

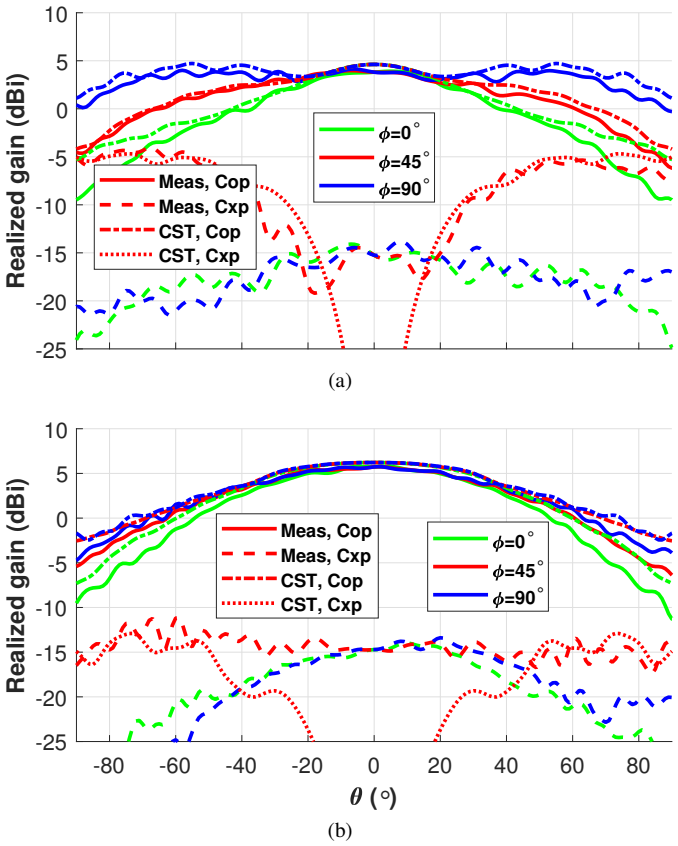


Fig. 24: Measured radiation pattern at 14.25 GHz for (a) EQA#1 and (b) EQA#2.

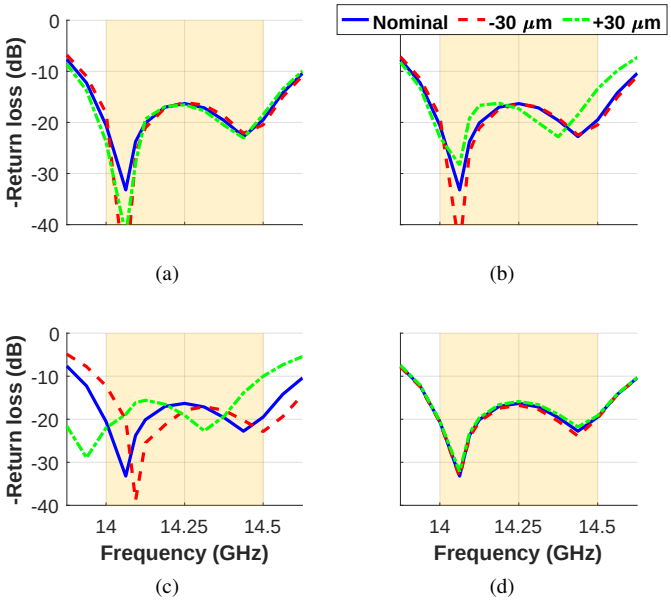


Fig. 25: Effect of the tolerances over the different design parameters on the return loss value of EQA#2: (a) a_{wg}, (b) w_r, (c) h_r, (d) l_{eva}.

TABLE III: Comparison of the EQA with other sub-wavelength periodicity solutions.

Parameter	EQA	[39]	[40]	[27]	[41]
f_0 (GHz)	14.25	11.70	14.25	100.00	34.00
Δ_{BW} (%)	6.7	17.5	7.0	20.0	26.3
Periodicity (λ_0)	0.54	0.60*	0.51	0.60	>0.83*
Scanning range (°)	±50	20-60	±75	±50	0
Dual polarization	Yes	No	Yes	No	Yes
Full metal	Yes	No	No	Yes	Yes
Efficiency (%)	93	72	87	89	90

* Estimated from the information in the paper.

is systematic (the three prototypes exhibit exactly the same shift), it could be calibrated out by adjusting the design prior to manufacturing.

As a final word, it is important to emphasize that the monolithic manufacturing approach followed for EQA#2 reports important advantages, especially when considering larger arrays. First of all, monolithic manufacturing eliminates performance issues due to misalignment or poor contact between the parts composing the device. Additionally, as it can be clearly appreciated in Fig. 21 (b), the volume of the device is significantly reduced, which has a drastic positive impact on the weight, cost and fabrication time of the device.

C. Comparison with other works in the state of the art

In order to put the performance of the EQA in perspective, the obtained results are now compared with other AAs in the state of the art. The following four references (some of them based on dielectric patches, since there are not many waveguide-based AAs with wide FoV in the literature) are selected [27], [39]–[41].

The main performance indicators of these antennas are collected in Table III. It must be emphasized that the results for the EQA relative to the scanning performance are simulated values, since no prototype of the complete array has been manufactured. However, the presented EQA efficiency does correspond to the measured efficiency of the prototype presented in section V-B. As it can be observed, the EQA reports larger efficiency (93% versus 72-89%) and a comparable FoV in relation to other solutions with beam steering capabilities in the state of the art. Moreover, the efficiency difference is specially pronounced when comparing with planar solutions.

In addition, no other solution achieves at the same time beam scanning, dual polarization and a full-metal implementation. Even very recent and innovative works in the field of full-metal sub-wavelength steerable arrays like [27] are limited to single-polarization operation. On the contrary, other full-metal designs like [41] present dual-polarization but their radiation pattern cannot be steered. In fact, if steering capabilities were to be implemented in the array proposed in [41], the GL-free FoV would be very limited due to its high periodicity.

VI. Conclusion

This work has addressed the problem of obtaining sub-wavelength array elements with dual polarization for active antennas (AAs) completely avoiding the use of dielectrics. Two waveguide radiators have been proposed. The first of

This article has been accepted for publication in IEEE Transactions on Antennas and Propagation. This is the author's version which has not been fully edited and content may change prior to final publication. Citation information: DOI 10.1109/TAP.2022.3198512

them is a miniaturized quad-ridge horn which is used as a benchmark since it seems to be the most evident solution to obtain dual-polarization operation. However, although valid for normal incidence, this design has not permitted to obtain an AA with a steerable radiation pattern due to the excitation of the first high order mode of the quad-ridge waveguide.

A new antenna concept based on the use of evanescent waveguide sections is proposed, the Evanescent Quad-ridge Antenna (EQA). The performance of the EQA is proven to be very good for AA applications, and its superiority is shown when compared with the mini-horn due to the avoidance of any spurious resonance in the operation band. Moreover, outside this band the EQA presents high rejection, which potentially allows to suppress the initial filter of the receiving chain in the feed. A complete design methodology for this new type of antenna has been developed.

Additionally, the spurious resonance affecting the mini-horn is explained from a circuit perspective. Such a phenomenon is inherent to dual-polarized radiation from quad-ridge apertures, and it is related to the excitation of the first high order mode. In the case of the EQA, the spurious phenomena is avoided since the cutoff frequency of such mode is kept away from the operation frequency band.

Finally, the EQA concept is validated experimentally by means of a demonstrator in Ku-band (for which three prototypes have been built and characterized) and the performance of this new antenna concept is compared with other works in the state of the art.

APPENDIX

Instead of simply observing the S-parameters of the antenna, it is decided to define some parameters that allow to show its performance when both vertical and horizontal modes are excited simultaneously and in quadrature (attaining CP). This way, the complete performance of the antenna can be fully described by analyzing less data (basically, the cuts from $\phi = 0^\circ$ to 45°). For this purpose, the antenna is considered to be connected to an ideal polarizer, as shown in Fig. 26. The S-parameters matrix of this polarizer is [42]:

$$S^{Pol} = \frac{1}{\sqrt{2}} \cdot \begin{bmatrix} 0 & 0 & 1 & -j \\ 0 & 0 & -j & 1 \\ 1 & -j & 0 & 0 \\ -j & 1 & 0 & 0 \end{bmatrix}. \quad (6)$$

It should be noted that the electrical ports 3 and 4 of this polarizer correspond with the same physical port, which interfaces with the input port of the antenna.

The antenna is defined by a scattering matrix of active S-parameters that are computed considering a perfect periodical environment. In this situation, it is possible to define the power reflected at the excited port as:

$$S_{11}^{Active} = \frac{1}{2}\left(S_{11}^{Ant} - S_{22}^{Ant} - j \cdot (S_{12}^{Ant} + S_{21}^{Ant})\right), \quad (7)$$

and the power reflected to the X-polarized port of the polarizer:

$$S_{21}^{Active} = \frac{1}{2}\left(S_{21}^{Ant} - S_{12}^{Ant} - j \cdot (S_{11}^{Ant} + S_{22}^{Ant})\right). \quad (8)$$

Additionally, the power radiated by the antenna aperture in Co- and X-polarizations (LHCP and RHCP, respectively) can be expressed as:

$$\text{Co-pol} = \frac{1}{2}\left(S_{41}^{Ant} - jS_{42}^{Ant} - jS_{31}^{Ant} - S_{32}^{Ant}\right), \quad (9)$$

$$\text{X-pol} = \frac{1}{2}\left(S_{41}^{Ant} - jS_{42}^{Ant} + jS_{31}^{Ant} + S_{32}^{Ant}\right). \quad (10)$$

Finally, the X-polarization discrimination (XPD) can be defined as

$$\text{XPD} = \frac{\text{Co-pol}}{\text{X-pol}}. \quad (11)$$

REFERENCES

[1] Y. Rahmat-Samii and A. C. Densmore, "Technology trends and challenges of antennas for satellite communication systems," *IEEE Transactions on Antennas and Propagation*, vol. 63, no. 4, pp. 1191–1204, 2015.

[2] H. Fenech, A. Sonya, A. Tomatis, V. Soumpholphakdy, and J. L. S. Merino, "Eutelsat Quantum: A game changer," in *33rd AIAA International Communications Satellite Systems Conference and Exhibition*.

[3] E. Amyotte, E. Choinière, Y. Demers, R. Horth, S. Larouche, B. Lemelin-Auger, A. Liang, S. Rheault, and S. Sierra-Garcia, "Low-cost steerable antennas for LEO and MEO satellites," in *2011 33rd ESA Antenna Workshop on Challenges for Space Antenna Systems*, ESA/ESTEC, Noordwijk, The Netherlands, 2011.

[4] B. Lejay and J.-P. Fraysse, "Front-end radiating modular architecture for direct radiating antenna applications," in *2021 15th European Conference on Antennas and Propagation (EuCAP)*, 2021, pp. 1–5.

[5] A. Bhattacharyya, *Phased Array Antennas: Floquet Analysis, Synthesis, BFNs and Active Array Systems*, ser. Wiley Series in Microwave and Optical Engineering. Wiley, 2006.

[6] J. L. Salazar Cerreno, "Dual-polarized radiating patch antenna," U.S. Patent US9 520 655B2, Dec. 13, 2016.

[7] P. Gorski, M. C. Vigano, and D. Llorens del Rio, "Developments on phased array for low-cost, high frequency applications," in *2017 11th European Conference on Antennas and Propagation (EUCAP)*, 2017, pp. 436–438.

[8] J. Navarro, "Affordable, multi-function flight-worthy airborne phased-array sensor," in *2020 IEEE/MTT-S International Microwave Symposium (IMS)*, 2020, pp. 829–832.

[9] D. Cavallo, W. H. Syed, and A. Neto, "Connected-slot array with artificial dielectrics: A 6 to 15 GHz dual-pol wide-scan prototype," *IEEE Transactions on Antennas and Propagation*, vol. 66, no. 6, pp. 3201–3206, 2018.

[10] X. Luo, J. Ouyang, Z.-H. Chen, Y. Yan, L. Han, Z. Wu, T. Yu, and K. Zheng, "A scalable Ka-band 1024-element transmit dual-circularly-polarized planar phased array for SATCOM application," *IEEE Access*, vol. 8, pp. 156 084–156 095, 2020.

[11] A. Mahanfar, S. Shamsinejad, S. K. Arani, S. Ebadi, E. YETISIR, P. S. T. Hoang, J. R. D. Luis, and N. Apaydin, "Antenna modules for phased array antennas," U.S. Patent US20 190 252 796A1, Aug. 15, 2019.

[12] *NIGHTINGALE I: Ka-band high-speed downlink payload*, CesiumAstro, Inc., 2020, rev. A. [Online]. Available: https://global-uploads.webflow.com/5fe306caa0a61675092c68dc/606b2e699386fc56eeb4da4e_Cesium%20Nightingale%201%20Datasheet.pdf

[13] D. Alvarez, D. Peña, A. Montesano, A. Zornoza, A. Rubio, D. Acevedo, P. J. Lopez-Mateos, L. F. de la Fuente, S. Arenas, C. Mique, and E. Villete, "HispaSat AG1 DRA-ELSA active antenna: RF designand performance," in *33rd ESA Antenna Workshop on Challenges for SpaceAntenna Systems*, Noordwijk, The Netherlands:ESA/ESTEC, Oct. 2011.

[14] E. Gandini, F. Silvestri, A. Benini, G. Gerini, E. Martini, S. Maci, M. C. Viganò, G. Toso, and S. Monni, "A dielectric dome antenna with reduced profile and wide scanning capability," *IEEE Transactions on Antennas and Propagation*, vol. 69, no. 2, pp. 747–759, 2021.

[15] T. Jaschke, H. K. Mitto, and A. F. Jacob, "An SIW fed dual-band and dual-polarized lens antenna at K/Ka-band," in *2017 47th European Microwave Conference (EuMC)*, 2017, pp. 62–65.

[16] D. Tran, M. Tian, and L. Ligthart, "Theory and practice of a novel miniature radiator: the microstrip-like antenna," in *Proceedings of MELECON '94. Mediterranean Electrotechnical Conference*, 1994, pp. 422–426 vol.2.

This article has been accepted for publication in IEEE Transactions on Antennas and Propagation. This is the author's version which has not been fully edited and content may change prior to final publication. Citation information: DOI 10.1109/TAP.2022.3198512

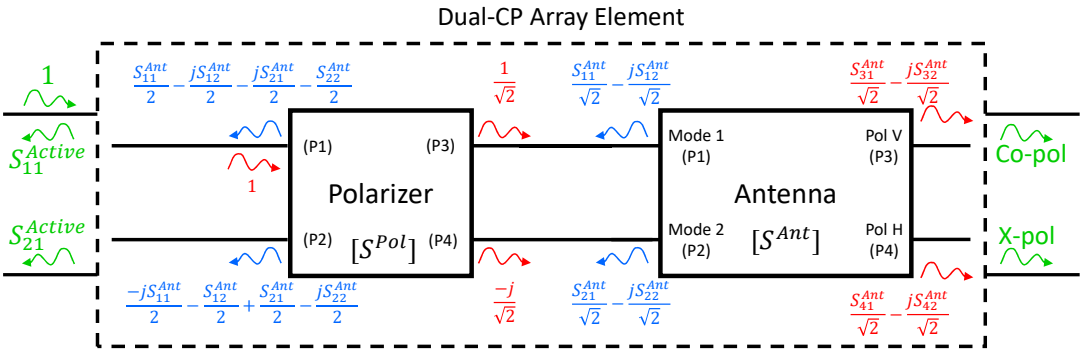


Fig. 26: Circuital representation of the proposed antenna (right block) cascaded with an ideal polarizer (left block). The incident and scattered waves are represented at each node of the circuit considering excitation at port 1 of the polarizer. Excitation of port 2 would give rise to the orthogonal radiated polarization. The scattering parameters S_{ij}^{Ant} correspond to the antenna block.

[17] P. Ludlow, V. Fusco, G. Goussetis, and D. Zelenchuk, "Small aperture evanescent-mode waveguide antenna matched using distributed coupled resonators," *Electronics Letters*, vol. 49, pp. 580–582(2), April 2013.

[18] Y. Song, Y. Wu, J. Yang, Y. Tian, W. Tong, Y. Chen, C. Wang, X. Tang, J. Benedikt, and K. Kang, "A compact Ka-band active integrated antenna with a GaAs amplifier in a ceramic package," *IEEE Antennas and Wireless Propagation Letters*, vol. 16, pp. 2416–2419, 2017.

[19] A. Maati, G. Mouchon, J. Belluot, P. Augoyat, M. Dinari, T. Huet, V. Serru, M. Camiade, and A. Katz, "Design and characterization of a Ka band 40 W RF chain based on GH15-10 GaN technology for space solid state power amplifier applications," in *2020 50th European Microwave Conference (EuMC)*, 2021, pp. 780–783.

[20] V. Pascale, D. Maiarelli, L. D'Agristina, and N. Gatti, "Design and qualification of Ku-band-radiating chains for receive active array antennas of flexible telecommunication satellites," *International Journal of Microwave and Wireless Technologies*, vol. 12, no. 6, p. 487–503, 2020.

[21] A. Montesano, L. de la Fuente, M. Bustamante, S. Arenas, D. Peña, E. Gonzalez, I. Herrera, F. Pacheco, A. Martin, J. Mora, M. Naranjo, C. Dirube, A. Gualo, A. Marcos, J. A. Rodriguez, P. Gomez, H. Fenech, S. Amos, F. Piro, A. L. Pera, I. Roberts, S. Weinberg, J.-P. Roux, A. M. Polegre, D. G. Otero, P. Gidney, and E. Granell, "ELSA+: An enabling technology for the flexibility and SW defined mission," in *38th ESA "Antenna Workshop onInnovative Antenna Systems and Technologies for Future Space Missions"*, Noordwijk, The Netherlands: ESA/ESTEC, Oct. 2017.

[22] B. Lejay, J. Rotureau, C. Giraudeau, N. Ferrando, D. Vynohradov, F. Michard, B. Lefebvre, F. Delahaye, A. Dechansiaud, J. P. Fraysse, E. Vourch, and G. Caille, "Front end radiating module development used in an advanced active antenna for future meo mission at thales alenia space," in *2020 14th European Conference on Antennas and Propagation (EuCAP)*, 2020, pp. 1–5.

[23] J. Montgomery, "Ridged waveguide phased array elements," *IEEE Transactions on Antennas and Propagation*, vol. 24, no. 1, pp. 46–53, 1976.

[24] E. Menargues, "Radiofrequency module," in *Patent WO2019229515A1*, 2018.

[25] Z. Yue, Y. Liu, and P. Zhu, "Design of a miniaturized double ridged horn antenna," in *2019 International Symposium on Antennas and Propagation (ISAP)*, 2019, pp. 1–2.

[26] E. G. Tianang, M. A. Elmansouri, and D. S. Filipovic, "Ultra-wideband lossless cavity-backed Vivaldi antenna," *IEEE Transactions on Antennas and Propagation*, vol. 66, no. 1, pp. 115–124, 2018.

[27] Y. Zhang, A. R. Vilenskiy, and M. V. Ivashina, "Wideband open-ended ridge gap waveguide antenna elements for 1-D and 2-D wide-angle scanning phased arrays at 100 GHz," *IEEE Antennas and Wireless Propagation Letters*, vol. 21, no. 5, pp. 883–887, 2022.

[28] C. Molero and M. García-Vigueras, "Circuit modeling of 3-D cells to design versatile full-metal polarizers," *IEEE Transactions on Microwave Theory and Techniques*, vol. 67, no. 4, pp. 1357–1369, 2019.

[29] D. Sánchez-Escuderos, J. Ruiz-Garnica, M. Baquero-Escudero, P. Soto, V. E. Boria, G. Toso, P. Angeletti, and M. Guglielmi, "Evanescent-mode ridge-waveguide radiating filters for space applications," *IEEE Transactions on Antennas and Propagation*, vol. 67, no. 10, pp. 6286–6297, 2019.

[30] V. Tornielli di Crestvolant and F. De Paolis, "Dimensional synthesis of evanescent-mode ridge waveguide bandpass filters," *IEEE Transactions on Microwave Theory and Techniques*, vol. 66, no. 2, pp. 954–961, 2018.

[31] D. A. Frickey, "Conversions between S, Z, Y, H, ABCD, and T parameters which are valid for complex source and load impedances," *IEEE Transactions on Microwave Theory and Techniques*, vol. 42, no. 2, pp. 205–211, 1994.

[32] P. Soto Pacheco, "Análisis y diseño optimizado de dispositivos pasivos de microondas de banda amplia con guías de sección transversal arbitraria," Ph.D. dissertation, Universitat Politècnica de València, Valencia, Spain, May 2012.

[33] F. Medina, F. Mesa, and R. Marques, "Extraordinary transmission through arrays of electrically small holes from a circuit theory perspective," *IEEE Transactions on Microwave Theory and Techniques*, vol. 56, no. 12, pp. 3108–3120, 2008.

[34] M. García-Vigueras, F. Mesa, R. Rodríguez-Berral, F. Medina, and J. R. Mosig, "Pseudo-analytical circuits for dual-polarized FSS," in *2016 10th European Conference on Antennas and Propagation (EuCAP)*, 2016, pp. 1–4.

[35] F. Mesa, R. Rodríguez-Berral, M. García-Vigueras, F. Medina, and J. R. Mosig, "Simplified modal expansion to analyze frequency-selective surfaces: An equivalent circuit approach," *IEEE Transactions on Antennas and Propagation*, vol. 64, no. 3, pp. 1106–1111, 2016.

[36] L. Polo-López, S. Sirci, A. Calleau, S. Capdevila, G. Toso, E. Menargues, and M. García-Vigueras, "Vertically printable evanescent mode filters," *IEEE Microwave and Wireless Components Letters*, (In press).

[37] E. Menargues, M. García-Vigueras, S. Capdevila, P. Angeletti, and G. Toso, "Meandered waveguides for active antennas," in *2021 15th European Conference on Antennas and Propagation (EuCAP)*, 2021, pp. 1–5.

[38] E. Menargues, "Radiofrequency component having a plurality of waveguide devices provided with ridges," in *Patent WO2020194270A1*, 2019.

[39] S. Vaccaro, D. L. del Río, R. T. Sánchez, and R. Baggen, "Low cost phased array for mobile Ku-band satellite terminal," in *Proceedings of the Fourth European Conference on Antennas and Propagation*, 2010, pp. 1–5.

[40] G. Gültepe, T. Kanar, S. Zihir, and G. M. Rebeiz, "A 1024-element Ku-band SATCOM phased-array transmitter with 45-dBW single-polarization EIRP," *IEEE Transactions on Microwave Theory and Techniques*, vol. 69, no. 9, pp. 4157–4168, 2021.

[41] F. Sun, Y. Li, J. Wang, Y. Ma, L. Ge, B. Ai, and R. He, "A millimeter-wave wideband dual-polarized antenna array with 3-D-printed air-filled differential feeding cavities," *IEEE Transactions on Antennas and Propagation*, vol. 70, no. 2, pp. 1020–1032, 2022.

[42] J. Uher, J. Bornemann, and U. Rosenberg, *Waveguide Components for Antenna Feed Systems: Theory and CAD*, ser. Artech House Antennas and Propagation Library. Artech House, 1993.

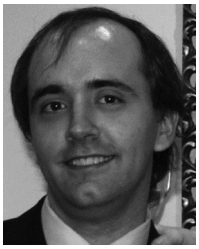
This article has been accepted for publication in IEEE Transactions on Antennas and Propagation. This is the author's version which has not been fully edited and content may change prior to final publication. Citation information: DOI 10.1109/TAP.2022.3198512



Lucas Polo-López received the B.Sc., M.Sc. and Ph.D. degrees in Telecommunication Engineering in 2014, 2016 and 2020 from the Universidad Autónoma de Madrid (UAM), Madrid, Spain respectively. He began collaborating with the Radiofrequency Circuits, Antennas and Systems (RFCAS) group of this same university in 2014, while he was doing his B.Sc. thesis. Since 2021 he is with the Institut d'Electronique et des Technologies du numéRique (IETR), working at the Institut National des Sciences Appliquées de Rennes (INSA Rennes) as a post-doctoral fellow. His current research interests include the conception of novel antenna arrays and its modelling by means of equivalent circuits, as well as the application of additive manufacturing techniques to the construction of antennas and waveguide devices. Dr. Polo-López has been recipient of two Best Ph.D. Thesis awards, one from COIT/AEIT and other from UAM, both in 2021 in Spain.



Esteban Menargues was born in Alicante, Spain, in February 1986. He received the M.Sc degree in electrical engineering from the Universidad Politécnica de Valencia (Valencia, Spain), in 2011. From 2011 to 2017, he was RF Engineer in Aurorasat (Valencia), Universidad Pública de Navarra (Pamplona, Spain), and the École Polytechnique Fédérale de Lausanne (Laussane, Switzerland). In 2017, he joined SWISSto12 SA (Renens, Switzerland), where he is currently Senior RF Engineer.



Santiago Capdevila was born in Barcelona, Spain. He received the M.Sc. and Ph.D. degrees in electrical engineering (with a minor in telecommunication engineering) from the Universitat Politécnica de Catalunya, Barcelona, in 2006 and 2013, respectively. In 2010, he joined the Department of Electrical and Computer Engineering, Henry Samueli School of Engineering, University of California at Irvine, Irvine, CA, USA, as a Visiting Scholar, under the FPU Fellowship Program. He was a Post-Doctoral Researcher with the Laboratory of Electromagnetics and Antennas, École Polytechnique Fédérale de Lausanne, Lausanne, Switzerland. He is currently Senior RF Engineer with SWISSto12 SA (Renens, Switzerland).



Giovanni Toso (S'93, M'00, SM '07) received the Laurea Degree (cum laude), the Ph.D. and the Post Doctoral Fellowship from the University of Florence, Italy, in 1992, 1995 and 1999. He spent more than one year as visiting scientist at the Laboratoire d'Optique Electromagnétique, Marseille (France). In 1999 he was a visiting scientist at the University of California (UCLA) in Los Angeles, he received a scholarship from Alenia Spazio (Rome, Italy) and he has been appointed researcher in a Radio Astronomy Observatory of the Italian National Council of Researches (CNR).

Since 2000 he is with the Antenna and Submillimeter Waves Section of the European Space Agency, ESA ESTEC, Noordwijk, The Netherlands. He has been initiating several R&D activities on satellite antennas based on arrays, reflectarrays, discrete lenses and reflectors. In particular, in the field of onboard satellite antennas, he has been coordinating activities on multibeam antennas (active and passive) mainly for Telecom Applications. In the field of terminal antennas for Telecom applications, he has been supporting the development of reconfigurable antennas with electronic, mechanical and hybrid scanning; some of these antennas are now available as products. He has promoted the development of the commercial software tool QUPES by TICRA, now used worldwide, for the analysis and design of periodic and quasi-periodic surfaces such as reflectarrays, frequency selective surfaces, transmitarrays and polarizers.

In 2014 he has been guest editor, together with Dr. R. Mailloux, of the Special Issue on "Innovative Phased array antennas based on non-regular lattices and overlapped subarrays" published in the IEEE Transactions on Antennas and Propagation and, for the same society, has been an Associate Editor (2013-2016). Since 2010, together with Dr. P. Angeletti, he has been instructing short courses on Multibeam Antennas and Beamforming Networks during international conferences (IEEE APS, IEEE IMS, IEEE IWCS, EUCAP, EuMW) that have been attended by more than 800 participants. In 2018 G. Toso has been the chairman of the 39th ESA Antenna Workshop on "Multibeam and Reconfigurable Antennas". In the same year he received, together with Prof. A. Skrivervik, the 2018 ESoA Best Teacher Award. G. Toso is the organiser of the new ESoA course on Active Antennas.



María García-Vigueras was born in Murcia, Spain. She received the M.Sc. degree in telecommunications engineering and the Ph.D. degree from the Technical University of Cartagena (Cartagena, Spain), in 2007 and 2012, respectively. From 2012 to 2015, she was a Research Fellow with the Laboratory of Electromagnetism and Antennas, École Polytechnique Fédérale de Lausanne (Lausanne, Switzerland). She is currently an Assistant Professor with the Institute National des Sciences Apliquées de Rennes (Rennes, France). She has coauthored more than 20 IEEE journals and 40 publications in international conferences. Her current research interests include leaky wave antennas, periodic surfaces, active antennas, waveguide feed chain components, and the evaluation of additive manufacturing's potential for RF design. Dr. García Vigueras was a recipient of several prizes, including two Best Ph.D. Thesis awards from COIT/AEIT in 2014 and UPTC in 2013, respectively, in Spain, and Best Paper Awards in MAPE 2013 in Chengdu, and EuCAP 2012 in Prague.